Supplementary Information (SI) for Energy & Environmental Science.

Supporting Information for

Nanoplex-Driven Energy Storage in Relaxor Antiferroelectrics

Simin Wang[&], Ke Xu[&], Guanglong Ge, Faqiang Zhang, Wangfeng Bai, Fei Yan, Jin Qian, Luomeng Tang, Yang Liu, Chao Sun, Zhongbin Pan, Bo Shen[*], Zhifu Liu[*], Houbing Huang[*], Jiwei Zhai[*]

[*] Corresponding Author.

E-mail addresses: shenbo@tongji.edu.cn (Bo Shen)
liuzf@mail.sic.ac.cn (Zhifu Liu)
hbhuang@bit.edu.cn (Houbing Huang)
apzhai@tongji.edu.cn (Jiwei Zhai)

& These authors contributed equally to this work and should be considered co-first authors.

This PDF file includes:

Figure S1 to S11
Table S1

Ceramic preparation

A group of (1-x)(0.75$NaNbO_3$-0.25$Bi_{0.5}Na_{0.5}TiO_3$)-x$Sr_{0.7}Bi_{0.2}TiO_3$ ceramic composites (denoted as NNBNT-xS, x = 0 - 0.10) were synthesized using a combination of solid-state reaction and tape-casting techniques. Starting reagents comprising bismuth oxide (Bi_2O_3, ≥99%), sodium carbonate (Na_2CO_3, ≥99.8%), strontium carbonate ($SrCO_3$, ≥99%), titanium dioxide (TiO_2, ≥98%), and niobium pentoxide (Nb_2O_5, ≥99.9%) from Sinopharm Chemical Reagent were stoichiometrically proportioned. These precursor compounds underwent homogenization through 12 h planetary ball milling with ethanol media, followed by dehydration at 80 °C and subsequent calcination at 850 °C for 4 h in alumina crucibles. The calcined product was subjected to secondary milling using zirconia balls, achieving particle size refinement before being blended with organic additives including polyvinyl butyral binder, dibutyl phthalate plasticizer, and glycerol trioleate dispersant in a solvent system of ethanol/butanone. This formulated slurry was cast into green tapes through doctor-blade deposition, with film thickness precisely controlled at 20 ± 1 μm by adjusting the blade gap. The cast film is cut, laminated, and cut, and placed in the isostatic press machine PTC LT08001 (EASEN) to hold at 75°C for 1 h. Prior to final sintering, the binder burnout procedure was executed through controlled thermal decomposition at 600 °C for 8 h. Densification was achieved via two-stage sintering: initial heating at 5 °C/min to 1250 °C followed by 2 h dwell, with optimal specimens requiring peak temperatures up to 1300 °C depending on composition

MLCCs Preparation

The manufacturing distinction of multilayer ceramic capacitors (MLCCs) primarily involves printing and lamination processes of cast film with electrodes, whereas other procedures align with standard ceramic processing. The film thickness of the MLCCs sample is 8 μm. The high-temperature Pd slurry is used as the inner electrode, and the MLCCs with five effective dielectric layers are fabricated by stacking process. The sintering process of the MLCC device is almost the same as that of the ceramic sample. The gold electrode is used as the terminal electrode for electrical performance testing. The MLCC devices are about 4 mm in length and 4 mm in width, respectively, and have an active electrode area of about 4 mm^2 in a single layer. Therefore, the total electrode active area of devices is about 20 mm^2.

Characterization

The microstructure was examined using a Field Emission Scanning Electron Microscope (FE-SEM, model FEI Nova NanoSEM 450). Transmission Electron Microscopy (TEM, model JEM-2100CX from JEOL, Japan) was employed to visualize the domain topography and diffraction patterns of the specimen. X-ray Diffraction (XRD) analysis, conducted with a Rigaku D/max 2550 V system utilizing Cu Kα radiation, facilitated phase identification. Local structural alterations were investigated via Raman spectroscopy, utilizing a Horiba JobinYvon HR800 spectrometer equipped with a Linkam THM600 heating stage, under 532 nm laser excitation. In the polarization-electric field (P-E) loop experiment, a sample with an electrode diameter of 2 mm and thickness around 20 μm was utilized. Ferroelectric properties were assessed through monopolar testing conducted on a Precision Premier II ferroelectric analyzer from Radiant Technologies, USA. Dielectric characteristics as functions of temperature and frequency were measured using an Agilent E4980A precision LCR meter coupled with a Tongguo Technology heating stage based in Shanghai, China. High-resolution imaging at the atomic scale was achieved through High-Angle Annular Dark-Field Scanning Transmission Electron Microscopy (HAADF-STEM) on a Hitachi HF5000 microscope operating at 200 kV, employing an Ultra-High Resolution (UHR) mode with a probe semi-angle range of 60-320 mrad. Displacement vectors associated with local displacements of A/B-site sublattices were computed by determining atomic positions via spherical Gaussian fitting of each atomic site, facilitated by an algorithm implemented in MATLAB software. During in situ testing, the ceramic's surface was coated with gold to mitigate Au signal interference; however, to minimize electrode sputtering effects on the measurement surface, the duration of sputtering was reduced.

Phase-field simulations

The electric field distribution and electric tree evolution were modelled using the finite element method with two-dimensional models in COMSOL software. The simulated model and parameters were based on the SEM diagrams with the selected size is 8.5×6 μm^2 and dielectric spectra. In the phase-field modeling for dielectric breakdown, the dielectric permittivity during the evolution process can be expressed as:

$$\varepsilon(s) = \frac{\varepsilon_{ini}}{f(s) + \mu} \tag{1}$$

where ε_{ini} represents the initial ε_r, $f(s) = 4s^3 - 3s^4$, and μ is 0.0001. The value of s which ranges from 0 to 1 is introduced to express the degree if damage in the breakdown behavior, corresponding the complete damage state to the intact state of the phase field. In this work, the main objects is ferroelectric ceramics, which contain multiple crystal grains. The ε_r of grains is electric field-dependent following Johnson's approximation, and the ε_r of grain boundary is linear. Therefore, the ε_r of grains (ε_g) and grain boundaries (ε_{gb}) under a specific electric field is described by the following equation:

$$\varepsilon_{ini}(E) = \frac{\varepsilon_g(0)}{(1 + kE^2)^{1/3}} \tag{2}$$

Where $\varepsilon_g(0)$ is the relative permittivity under a zero-field, which is taken to be different ceramics. The parameter $k = 3\beta\varepsilon_{gb}^3$ is the attenuation coefficient of the relative permittivity with variation of an electric field. β linearly affects the degree to which the relative permittivity varies with an electric field. The degree to which the relative permittivity of different ferroelectric materials decays with increasing electric field varies.[1-3] Here, we set β to 1 to represent a material whose relative permittivity change smoothly with the electric field. ε_{gb} is a relative value used for calculating the relative permittivity of different crystal phases, which is set to 1 as the relative permittivity of air. Combining Equations (1) and (2), an equation representing the dielectric permittivity during the breakdown behavior can be obtained:

$$\varepsilon(E{,}s) = \frac{\varepsilon_g(0)}{(f(s) + \mu)(1 + kE^2)^{\frac{1}{3}}} \tag{3}$$

In the model, the evolution of breakdown behavior is mainly based on energy. The total potential energy of system can be expressed as:

$$\prod[s\,x_i] = \int_\Omega [W_e(E, s) + W_d(s) + W_i\left(\frac{\partial s}{\partial x_i}\right)]d V \tag{4}$$

W_e, W_d and W_i are complementary electrostatic potential energy per unit volume, the damage energy, and a gradient energy term respectively. W_e in crystal phase can be expressed as:

$$W_e(E, s) = -\int_0^{E_{max}} \frac{\varepsilon_0\varepsilon_g(s)E}{(1 + kE^2)^{\frac{1}{3}}} d E \tag{5}$$

and the damage energy can be described as $W_d(s) = W_c[1 - f(s)]$, where W_c is the critical density of electrostatic energy. The gradient energy term W_i used to adjust the sharp phase boundaries as:

$$W_i\left(\frac{\partial s}{\partial x_i}\right) = \frac{\Gamma \partial s}{4\partial x_i} \cdot \frac{\partial s}{\partial x_i} \tag{6}$$

where Γ can be approximated as breakdown energy.

By assuming the linear dynamic equation: $\frac{\partial s}{\partial t} = -m\frac{\delta \Pi}{\delta s}$, we can get the normalized dimensionless governing equation of breakdown propagation for nonlinear dielectric:

$$\frac{\partial}{\partial x_i}\left[\varepsilon_g(s)\left(1 + \frac{\partial\bar{\varphi}\partial\bar{\varphi}}{\partial\bar{x}_i\partial\bar{x}_i}\bar{k}\right)^{-\frac{1}{3}}\frac{\partial\bar{\varphi}}{\partial\bar{x}_i}\right] = 0 \tag{7}$$

$$\frac{\partial s}{\partial \bar{t}} = -\frac{3\varepsilon_g'(s)}{4\bar{k}}\left(\left(1 + \frac{\partial\bar{\varphi}\partial\bar{\varphi}}{\partial\bar{x}_i\partial\bar{x}_i}\bar{k}\right)^{\frac{2}{3}} - 1\right) + f'(s) + \frac{1}{2}\frac{\partial^2 s}{\partial\bar{x}_i\partial\bar{x}_i} \tag{8}$$

In equations (7) and (8), $\bar{k}$ is a nonlinear factor, and the variable marked with a horizontal line is the dimensionless counterpart of the corresponding quantity.

Polarization evolution model

NaNbO$_3$-based antiferroelectric is taken as an example by solving the TDGL equation for the temporal evolution of the polarization vector field,

$$\frac{\partial P_i(r,t)}{\partial t} = -L\frac{\delta F}{\delta P_i(r,t)}, (i = 1,2,3)$$ * MERGEFORMAT (1)

where $P_i(r,t)$ is polarization, L is the kinetic coefficient, and F is the total free energy of the system, which is expressed as,

$$F = \iiint (f_{Land} + f_{elas} + f_{elec} + f_{grad})dV$$ * MERGEFORMAT (2)

where V is the system volume. The Landau free energy density f_{Land} can be calculated by,

$$f_{Land} = \alpha_1(P_1^2+P_2^2+P_3^2)+\alpha_{11}(P_1^4+P_2^4+P_3^4)+\alpha_{12}(P_1^2P_2^2+P_1^2P_3^2+P_2^2P_3^2)$$
$$+\alpha_{112}\left[P_1^4(P_2^2+P_3^2)+P_2^4(P_1^2+P_3^2)+P_3^4(P_1^2+P_2^2)\right]$$
$$+\alpha_{111}(P_1^6+P_2^6+P_3^6)+\alpha_{123}P_1^2P_2^2P_3^2$$

* MERGEFORMAT (3)

where P_1, P_2, P_3 are polarization components. α_1, α_{11}, α_{12}, α_{111}, α_{112} and α_{123} are Landau coefficients. The elastic energy density can be expressed as,

$$f_{elas} = \frac{1}{2}C_{ijkl}(\varepsilon_{ij}-\varepsilon_{ij}^0)(\varepsilon_{kl}-\varepsilon_{kl}^0)$$

* MERGEFORMAT (4)

where C_{ijkl} is the elastic stiffness tensor, ε and ε^0 are the total local strain, and the eigenstrain, respectively. The gradient energy density can be expressed as,

$$f_{grad} = \sum_i \left\{ \lambda_0 \left[\left(\frac{\partial P_i}{\partial x}\right)^2 + \left(\frac{\partial P_i}{\partial y}\right)^2 \right] + g_0 \left[\left(\frac{\partial^2 P_i}{\partial x}\right)^2 + \left(\frac{\partial^2 P_i}{\partial y}\right)^2 \right] \right\}$$

* MERGEFORMAT (5)

where $i = 1, 2, 3$. λ_0 is a negative constant, which favors the stability of the AFE phase. g_0 is a positive constant, which drives the phase transition from AFE to FE[4]. In this work, $\lambda_0 = -3.5\, a_c^2 \times 10^7$, $g_0 = 0.6\, a_c^4 \times 10^7$. The electrostatic energy density f_{elec} is given by,

$$f_{elec} = -P_i(r)E_i^{ex}(r) - \frac{1}{2}P_i(r)E_i^{in}(r)$$

* MERGEFORMAT (6)

where E^{ex} is the external electric field, E^{in} is the internal electric field, including dipole-dipole interaction field and local electric field caused by the random point defects.

The equation was solved by a semi-implicit Fourier spectral method and the simulation size is 256 Δx × 256 Δy × 1 Δz. (Δx = a_c is the number of grids points and equals 0.5 nm in this work) For mechanical boundary conditions of $NaNbO_3$-based bulk is periodic. We use Landau coefficients of the $NaNbO_3$-based system for the calculation[5], which is available as follows. For the matrix, $\alpha_1 = -6.5\times10^7$ J m C^{-2}, $\alpha_{11} = 0.9\times10^8$ J m^5 C^{-4}, $\alpha_{12} = 8\times10^8$ J m^5 C^{-4}, $\alpha_{111}=3.3\times10^9$ J m^9 C^{-6}, $\alpha_{112} = -3.5\times10^9$ J m^9 C^{-6}, $\alpha_{123} = -1.0\times10^9$ J m^9 C^{-6}, $\alpha_{1111} = 3.1\times10^{10}$ J m^{13} C^{-8}, $\alpha_{1112} = 0.2\times10^{10}$ J m^{13} C^{-8}, $\alpha_{1122} = 4.2\times10^{10}$ J m^{13} C^{-8}, $\alpha_{1123} = -5.0\times10^{10}$ J m^{13} C^{-8}. $C_{11} = 2.3\times10^{11}$ J m^{-3}, $C_{12} = 0.9\times10^{11}$ J m^{-3}, $C_{44} = 0.76\times10^{11}$ J m^{-3}, $Q_{11} = 0.16$ m^4 C^{-2}, $Q_{12} = -0.072$ m^4 C^{-2}, $Q_{44} = 0.084$ m^4 C^{-2}. For the paraelectric phase, $\alpha_1 = 6\times10^7$ J m C^{-2}, $\lambda_0 = 0.6\, a_c^2 \times 10^7$and $g_0 = 0$[6].

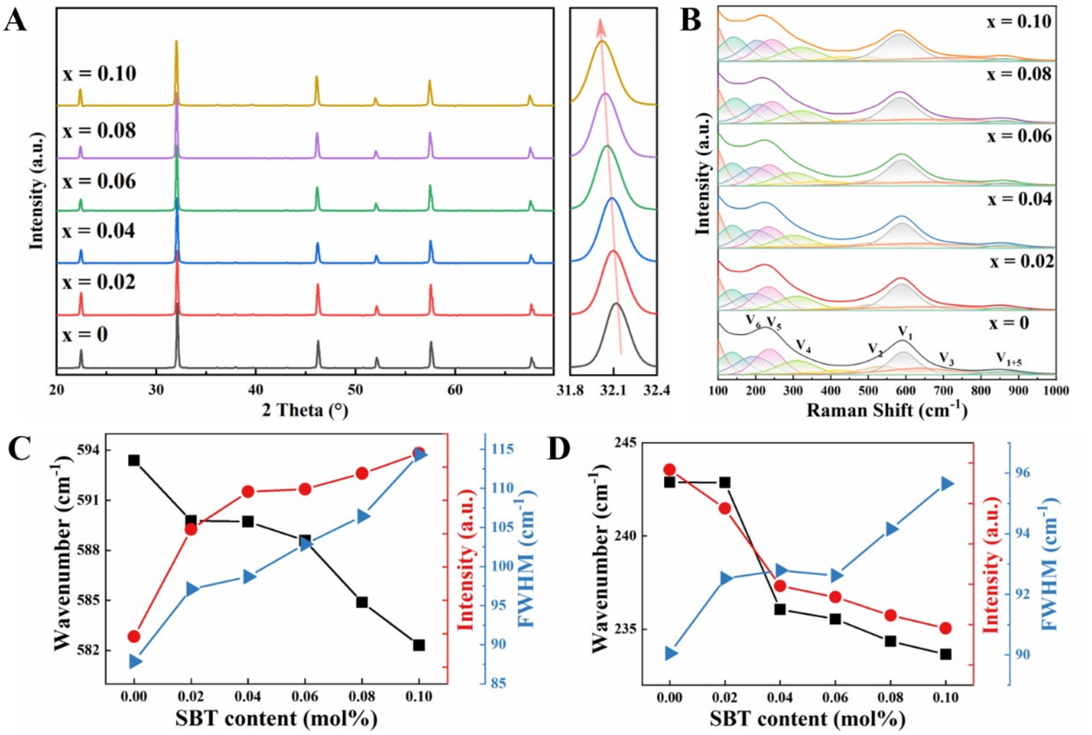

Fig. S1. (A) X-ray diffraction pattern of NNBBT-xS ceramics at room temperature. (B) Raman spectroscopy of NNBBT-xS ceramics at room temperature. Wavenumber, intensity, and width of (C) V_1 and (D) V_5 peaks in Raman spectra of NNBBT-xS ceramics at room temperature.

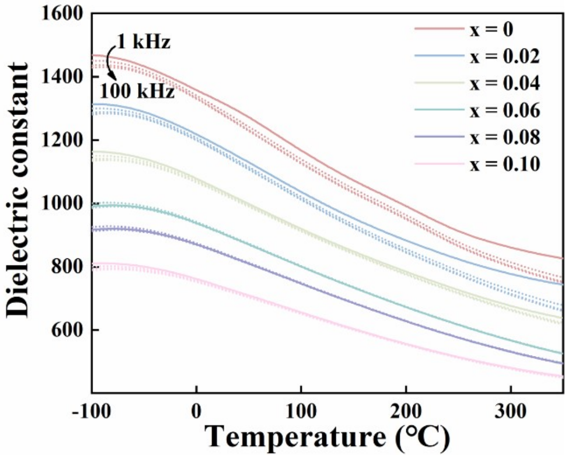

Fig. S2. The change in the value of the dielectric constant at different frequencies

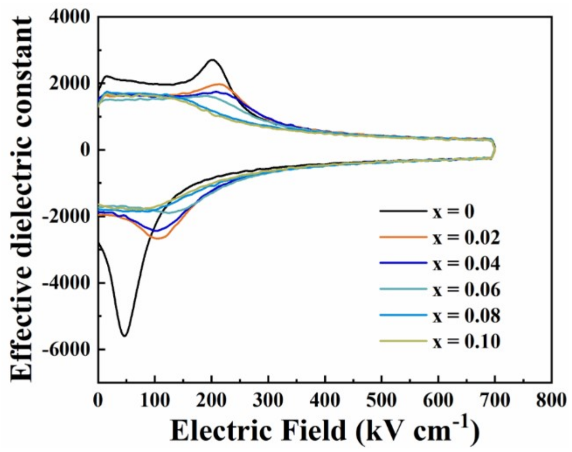

Fig. S3. Current curves of x at 700 kV cm^{-1} electric field.

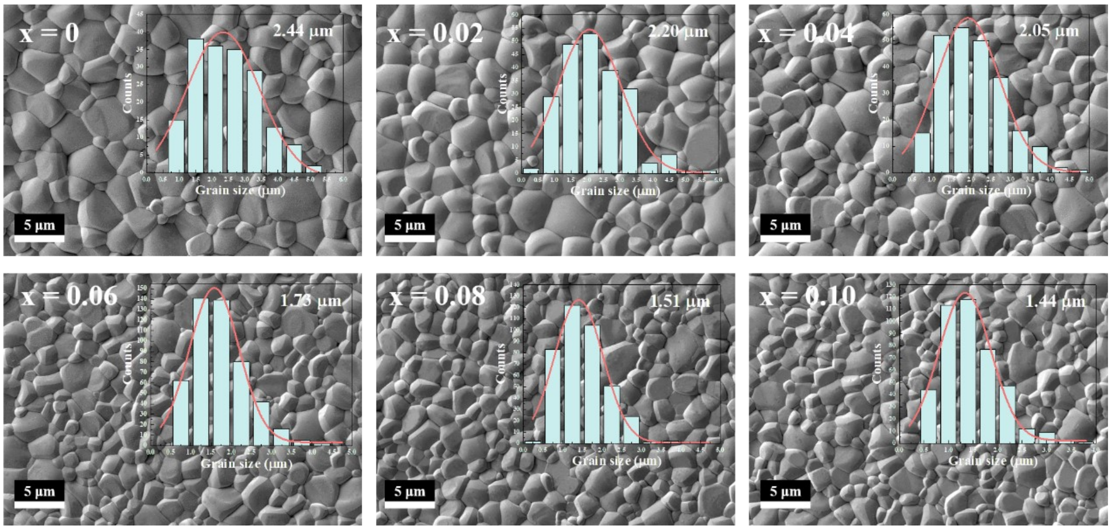

Fig. S4. The SEM of NNBBT-xS ceramics.

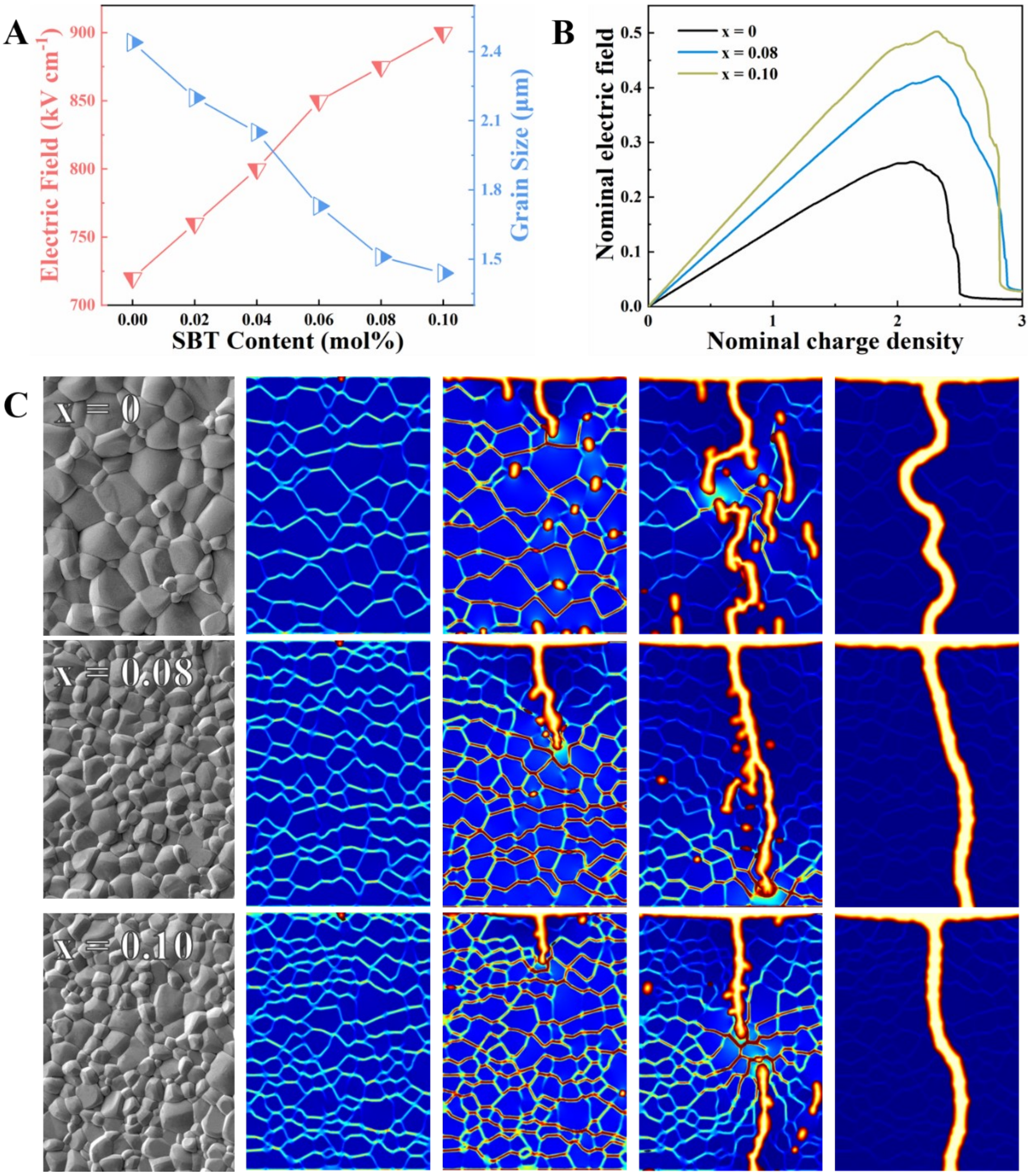

Fig. S5. (A) Grain size and breakdown field strength with different x. (B) Nominal electric field of x = 0, x = 0.08 and 0.10 ceramics. (C) Phase-field simulations of the final breakdown paths for samples x = 0, x = 0.08 and 0.10.

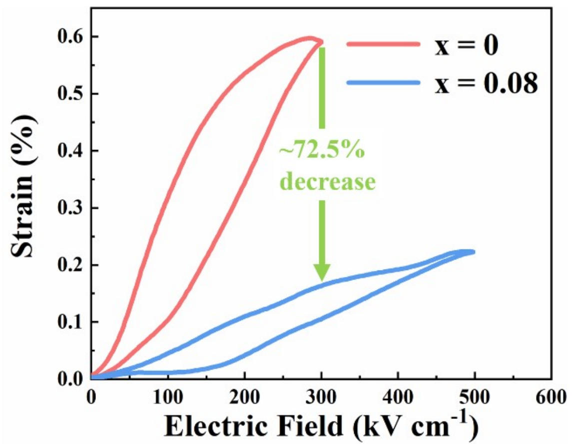

Fig. S6. Strain-electric field (S-E) curves of the x = 0 and 0.08 ceramics.

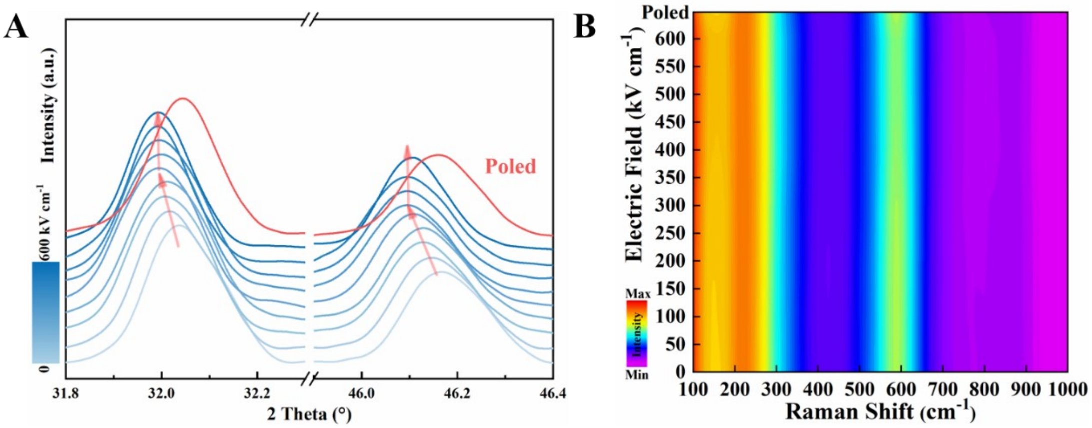

Fig. S7. In situ electric field XRD and Raman spectra for the x = 0.08 ceramics.

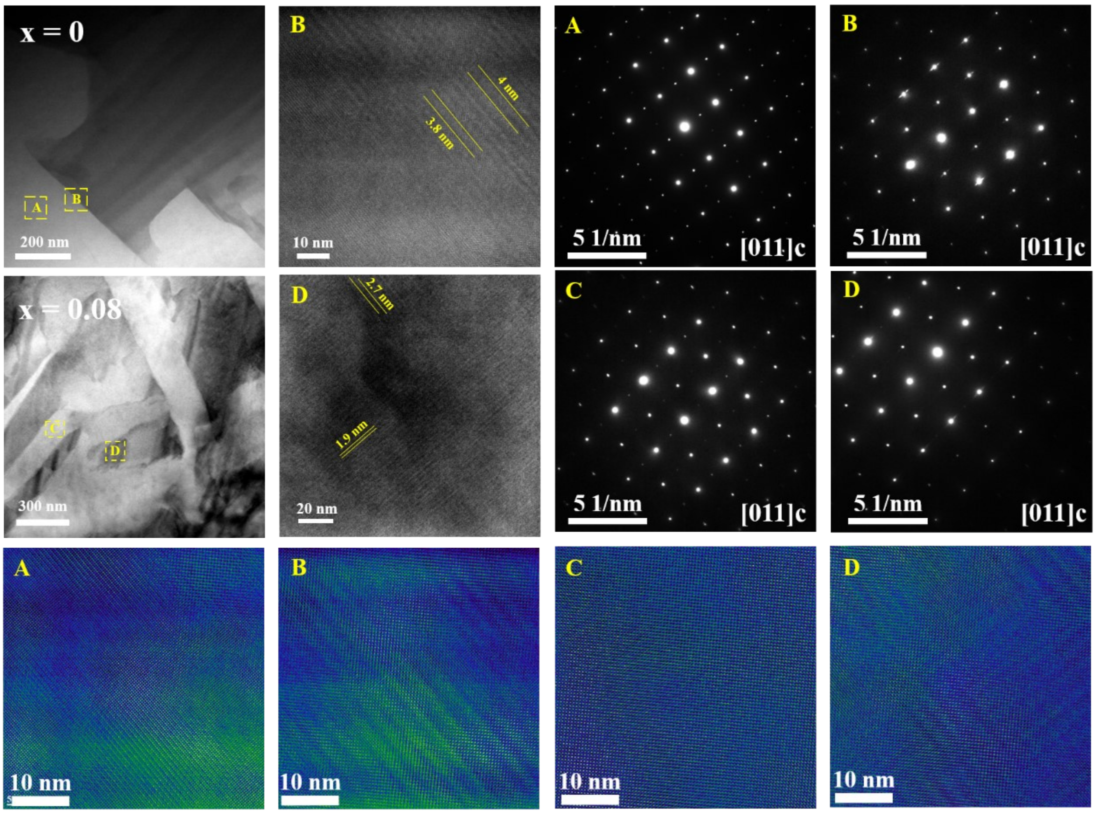

Fig. S8. Domain morphology and SAED for the ceramics with components x = 0 and 0.08.

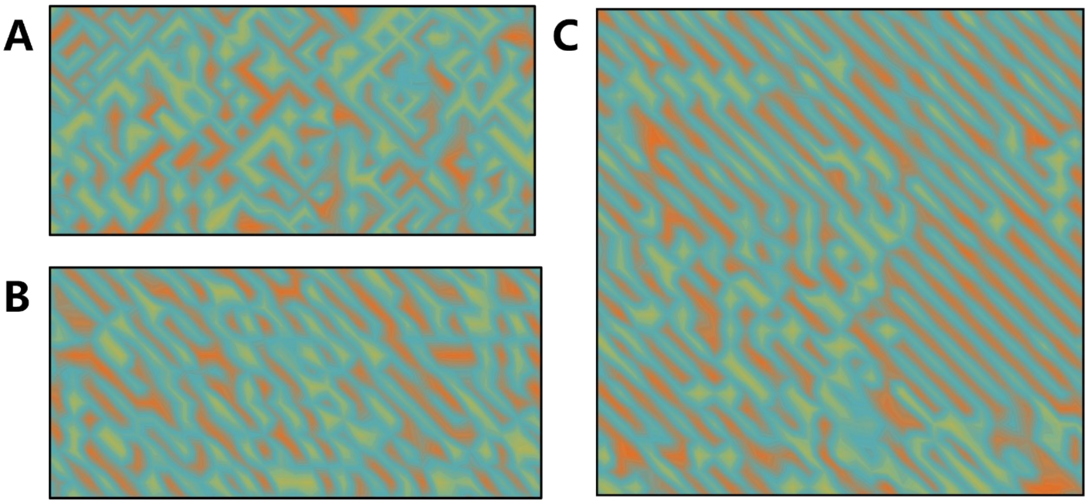

Fig. S9. Two-dimensional contours of polarization angles polarization magnitudes of (A) the 1/2 diffraction spot region with x = 0, (B) the 1/2 diffraction spot region with x = 0.08, and (C) the 1/6 diffraction spot region with x = 0.08.

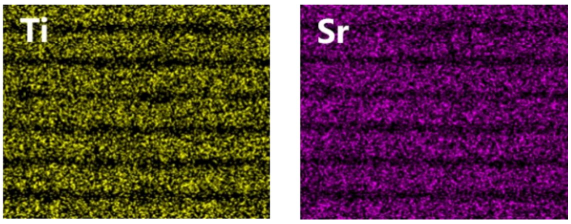

Fig. S10. Digital representation of the MLCCs image of the cross-sectional area with corresponding element distribution

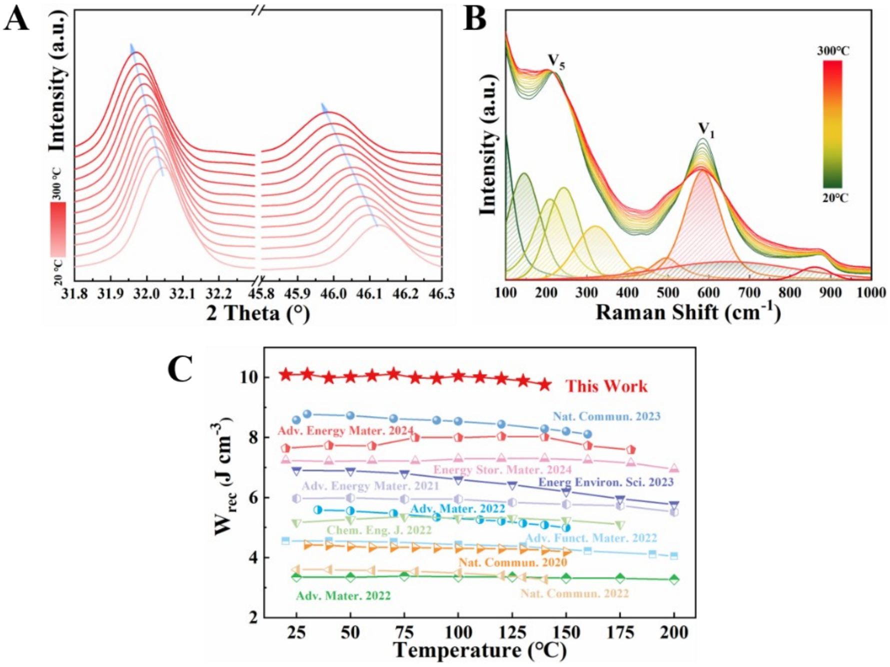

Fig. S11. In situ temperature field (A) XRD and (B) Raman spectra for the x = 0.08 ceramics. (C) Contrast the temperature stability of the NN-based MLCCs presented herein with those of recently reported energy storage ceramic materials.

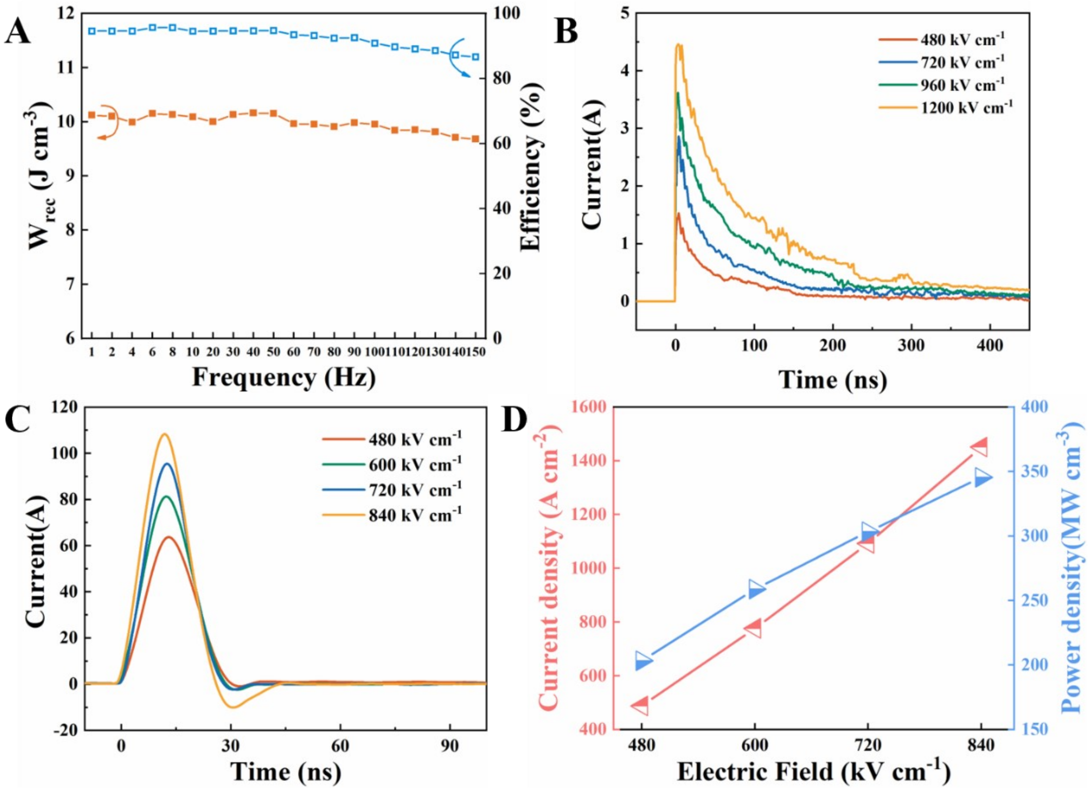

Fig. S12. (A) Frequency response of the material were examined at a high electric field strength of 800 kV cm^{-1}. (B) Overdamped and (C) underdamped circuits. (D) Power density and an effective current density under underdamped circuits.

Table S1. Summary of XRD refinement parameters of NNBBT-xS ceramics

Component	Space group	Lattice parameters	V (Å^3)	R$_{wp}$ (%)	R$_p$ (%)
x = 0	Pnma	a=7.79329 Å^3, b=7.79331 Å^3, c=23.35423 Å^3 α=β=γ=90°	1418.43	5.93	3.91
x = 0.02		a=7.79172 Å^3, b=7.791476 Å^3, c=23.38560 Å^3 α=β=γ=90°	1419.72	5.78	3.82
x = 0.04		a=7.80111 Å^3, b=7.80112 Å^3, c=23.37738 Å^3 α=β=γ=90°	1422.69	5.73	3.85
x = 0.06		a=5.54421 Å^3, b=7.80130 Å^3, c=23.37915 Å^3 α=β=γ=90°	1422.85	5.68	3.73
x = 0.08		a=7.80224 Å^3, b=7.80248 Å^3, c=23.38046 Å^3 α=β=γ=90°	1423.33	5.73	3.71
x = 0.10		a=7.80567 Å^3, b=7.80565 Å^3, c=23.40311 Å^3 α=β=γ=90°	1425.91	6.12	3.96

Reference

[1] Z. Cai, X. Wang, W. Hong, B. Luo, Q. Zhao, L. Li, *J. Am. Ceram. Soc*. **2018**, 101, 5487–5496.

[2] Z. Cai, X. Wang, B. Luo, W. Hong, L. Wu, L. Li, *J. Am. Ceram. Soc*. **2018**, 101, 1607–1615.

[3] K.M. Johnson, *J. Appl. Phys.* **1962**, 33, 2826–2831.

[4] K. Xu, X. Shi, C. Shao, S. Dong, H. Huang, *npj Comput. Mater.* **2024**, 10, 150.

[5] B. Lin, K. Ong, T. Yang, Q. Zeng, H. Hui, Z. Ye, C. Sim, Z. Yen, et al, *Nature*. **2024**, 633, 798-803.

[6] J. Wang, Z. Zheng, L. Zhao, J. Zhang, X. Fan, Z. Liu, K. Zhu, Q. Yuan et al, *J. Mater. Chem. A*. **2023**, 11, 22512.